Regulated nuclear accumulation of a histone methyltransferase times the onset of heterochromatin formation in *C. elegans* embryos

Beste Mutlu[1], Huei-Mei Chen[1], James J. Moresco[2], Barbara D. Orelo[2], Bing Yang[3], John M. Gaspar[4], Sabine Keppler-Ross[1,6], John R. Yates III[2], David H. Hall[5], Eleanor M. Maine[3], Susan E. Mango[1,6*].

Affiliations:

[1] Department of Molecular and Cellular Biology, Harvard University, Cambridge, MA

[2] Department of Chemical Physiology, The Scripps Research Institute, La Jolla, San Diego, CA, USA

[3] Department of Biology, Syracuse University, New York 13244

[4] Informatics Group, Faculty of Arts and Sciences, Harvard University, Cambridge MA, USA

[5] Center for C. elegans Anatomy, Albert Einstein College of Medicine, Bronx, NY

[6] current address: Biozentrum, University of Basel, 4056 Basel, Switzerland

*Correspondence to: smango@mcb.harvard.edu

Keywords: SETDB1, PCOS, polycystic ovarian syndrome, melanoma, lung, *met-2*

ONE SENTENCE SUMMARY: MET-2/SETDB1 and interactors LIN-65/ATF7IP and ARLE-14/ARL14EP initiate heterochromatin formation during embryogenesis.

ABSTRACT

Heterochromatin formation during early embryogenesis is timed precisely, but it has been elusive how this process is regulated. Here we report the discovery of a histone methyltransferase complex whose nuclear accumulation and activation establishes the onset of heterochromatin formation in *C. elegans* embryos. We find that the inception of heterochromatin generation coincides with the accumulation of the Histone H3 Lysine 9 (H3K9) methyltransferase MET-2 (SETDB) into nuclear hubs. The absence of MET-2 results in delayed and disturbed heterochromatin formation, whereas accelerated nuclear localization of the methyltransferase leads to precocious H3K9 methylation. We identify two factors that bind to and function with MET-2: LIN-65, which resembles ATF7IP, localizes MET-2 into nuclear hubs, and ARLE-14, orthologous to ARL14EP, promotes stable association of MET-2 with chromatin. These data reveal that nuclear accumulation of MET-2 in conjunction with LIN-65 and ARLE-14 regulates timing of heterochromatin domains during embryogenesis.

INTRODUCTION

The nucleus of a young embryo undergoes major reorganization as it transitions from a fertilized egg to a multicellular embryo. As cells acquire specific fates and zygotic transcription commences, the nucleus is segregated into distinct domains of euchromatin and heterochromatin (*1*). While much has been learned about the mechanisms that control cell-fate specification and the onset of zygotic transcription (*2*, *3*), little is understood about the processes that establish chromatin domains *de novo* during embryogenesis.

Heterochromatin domains are generated *de novo* during development (*1*). In early mouse embryos, embryonic stem cells and planarian neoblasts, higher-order heterochromatin is lacking, but becomes established as these cells differentiate. Their nuclei shrink, chromatin compacts, and the nucleoplasm becomes divided into visible domains of euchromatin and heterochromatin (*1*, *4*). In *C. elegans*, the dynamics of embryonic chromatin has been tracked with artificial chromosomes. These appear large and distended at the earliest stages of embryogenesis and undergo compaction during gastrulation (*5*, *6*). These examples suggest that the segregation of heterochromatin domains is a conserved feature of the differentiated state. Little is known, however, what drives formation of heterochromatin during embryogenesis or what determines the timing of chromatin reorganization.

Here, we characterize the regulation of MET-2 protein and its relation to heterochromatin formation during embryogenesis. We identify partner proteins that mediate MET-2 subcellular localization and chromatin association. We find that MET-2

and its partners are critical for the timely generation of heterochromatin during embryogenesis.

RESULTS

We began our analysis with a survey of wild-type embryos using two assays for heterochromatin: First, we used transmission electron microscopy (TEM). TEM studies since the 1960s have shown that heterochromatin domains can be detected as electron-dense regions (EDRs), and that heterochromatin-associated histone modifications such as H3K9me are located within EDRs (*7–10*). Second, we surveyed histone modifications by antibody stains, to track their abundance and distribution in early embryos. Histone modifications are associated with active or silent regions of the genome, and can be a hallmark of heterochromatin (*11*).

By TEM, nuclei in the youngest embryos appeared relatively homogenous, with light speckling in the nucleoplasm and a nuclear envelope free of electron-dense material (Fig. 1A-B). Upon initiation of gastrulation (~21-50 cell stage), embryos gained more electron-dense puncta throughout their nuclei. By mid-gastrulation (51-100 cell stage), dark material was observed abutting the nuclear envelope, and the nucleoplasmic puncta coalesced into larger, but fewer, electron-dense compartments. These features became more pronounced over time, with large EDRs that spanned the nucleus and bordered the nuclear periphery (Fig. 1B, >200 cells). We note that EDRs appeared throughout the embryo, suggesting that cells destined to produce different cell types nevertheless generated heterochromatin domains at about the same time in development (fig. S1A).

We surveyed histone modifications to determine if they were dynamic during development. There was a dramatic increase in Histone H3 Lysine 9 methylation (H3K9me) from fertilization to the mid-gastrula in interphase cells. We quantified the effect, using antibodies against histone H3 to normalize (see Methods). H3K9me2 increased ten-fold ($p=4x10^{-19}$), while H3K9me1 increased two-fold (p=0.001), and H3K9me3 increased six-fold ($p=4x10^{-7}$; Fig. 1C, D). H3K9me2 was barely detectable at fertilization, consistent with prior studies that showed H3K9me2 is erased in the germ line and undetectable in oocytes (*12*). Bright H3K9me2 puncta became apparent by the 20-cell stage throughout embryonic nuclei. The signal intensified during gastrulation, with more puncta and brighter staining within puncta (~51-100-cell stage, mid-stage). A time series of whole embryo stains indicated that most interphase nuclei behaved similarly (fig. S1B), and two different antibodies against H3K9me2 gave identical results (fig. S1C). Controls indicated that the signal was specific because mutants lacking H3K9me2 (*12*, *13*) failed to stain with any of the H3K9me2 antibodies (fig. S1D-E). Both puncta of histone modifications and EDRs arose during gastrulation, suggesting H3K9me stains are a useful proxy to visualize heterochromatin domains.

Not all histone modifications were developmentally regulated (Fig. 1C, fig. S1B). The Polycomb-mediated modification H3K27me3 was abundant in early embryos and did not increase further, as observed previously (*14*). This result indicates that H3K27me3 is not sufficient for higher-order heterochromatin. Pan H4 acetylation, a modification associated with active chromatin, was present in early embryos before the onset of zygotic transcription and increased slightly over time. This observation reveals that bulk

loss of H4Ac is not required for higher-order heterochromatin. In short, only some modifications were regulated dynamically during embryogenesis.

To identify the molecular basis of heterochromatin formation, we focused on the methyltransferase MET-2. MET-2 is homologous to vertebrate SETDB1 (*15*, *16*), and required for virtually all H3K9me1 and H3K9me2, and for some H3K9me3 (*12*, *13*). We focused on H3K9me2 and MET-2 because H3K9me2 was regulated most dynamically during embryogenesis, because it promotes H3K9me3 (*12*), and because its location in the genome, by ChIP, tracks well with canonical heterochromatin proteins such as HPL-2/HP1 (*17*).

We asked whether loss of MET-2 impacted heterochromatin domains visible by TEM. Pre-gastrula *met-2* embryos matched their wild-type counterparts, with homogeneous, translucent nuclei (Fig. 2A). However, the speckles observed in wild-type nuclei at the 20-cell stage were dimmer in *met-2* mutants, and they failed to coalesce into EDRs by the 50-100-cell stage (Fig. 2A). EDRs emerged in older embryos, but they occupied less nuclear volume and were reproducibly paler than the wild type (Fig. 2A). We performed line-scan analysis to quantify the appearance of nuclear EDRs. The standard deviation of line-scan values is higher in nuclei with EDRs compared to homogeneous nuclei because the dark EDRs contrast with the pale nucleoplasm. *met-2* nuclei had a more homogeneous distribution of signal and a smaller standard deviation at every stage (Fig. 2B). To assess the amount of residual electron density in *met-2* late embryonic nuclei (>200 cell stage), we used an intensity threshold to define EDRs in wild-type and *met-2* embryos (Fig. 2C). The percentage of pixels in EDRs was reduced almost three-fold in *met-2* mutants compared to the wild type (Fig. 2C). To control for TEM

fixation and sectioning, we examined cytoplasmic organelles and yolk droplets. Intensity thresholding revealed that electron-dense cytoplasmic structures were present in *met-2* mutants (Fig. 2D) and they resembled those in wild-type embryos (fig. S2A, B). These results indicate that *met-2* is critical for the timely formation of segregated heterochromatin domains.

Given the dependence of H3K9me2 on MET-2, we asked if expression of MET-2 tracked with the onset of H3K9me2. MET-2 protein gradually shifted from the cytosol to the nucleus, from the 2-cell stage to the onset of gastrulation. This change was observed for both endogenous MET-2 and single-copy MET-2 reporters (Fig. 3A-C, fig. S3B-C). In 1-8-cell embryos, MET-2 was distributed throughout nuclei and cytoplasm with little nuclear accumulation. As embryos aged, the concentration of MET-2 within nuclei increased approximately five-fold (Fig. 3B, p=0.0002), whereas the absolute level of MET-2 protein did not change significantly over time (Fig. 3C). We note that early embryos had increased nuclear MET-2 and H3K9me2 transiently during prophase (fig. S3C, F), but we focus on interphase nuclei here.

These data may help resolve a controversy regarding where MET-2 is localized within cells (*13*, *18–20*). A previous study had concluded that MET-2 was cytosolic (*13*), whereas other work had suggested that MET-2 associated with chromatin (*19*) in the nucleus (*20*). Our data reveal that MET-2 transitions from the cytosol to the nucleus (Fig. 3A), a process that is regulated by its binding partner LIN-65 (see below and Discussion).

Given that *met-2* is necessary for heterochromatin domains, and that H3K9me2 accumulated dynamically in early embryos, we asked whether regulation of MET-2 constituted part of the embryonic timer for heterochromatin establishment. We

hypothesized that if nuclear MET-2 was rate-limiting, then premature accumulation of MET-2 in nuclei would lead to precocious H3K9me2 and initiate heterochromatin. We added a nuclear localization signal (NLS) from c-Myc to a FLAG-tagged copy of endogenous MET-2 using Crispr and examined embryos for H3K9me2 and histone H3 (a control for staining). We note that H3 appears to be released during mitosis, but our quantitation focused only on interphase cells.

Addition of an NLS resulted in a two-fold increase in nuclear MET-2 in pre-gastrula embryos (Fig. 3D, G). Increased nuclear MET-2 led to precocious accumulation of H3K9me2, beginning at least one cell division earlier than wild-type embryos (Fig. 3E, F, H; $p<0.05$ at all stages). These results suggest that gradual accumulation of MET-2 within nuclei initiates H3K9me2.

To understand how MET-2 is regulated, we searched for binding partners using immunoprecipitation followed by Multidimensional Protein Identification Technology Mass Spectrometry, using MET-2::GFP and 3xFLAG::MET-2. Wild-type *C. elegans* bearing no tagged proteins, and strains bearing an unrelated GFP or FLAG reporter served as negative controls. Results of our MET-2::GFP proteomics analysis can be found in Supplementary Table 1. We chose a candidate list of interacting partners based on the specificity of MET-2 binding, on the peptide counts and on protein coverage. We undertook a secondary screen for the effects of these candidates on H3K9me2. From this survey, two proteins emerged as likely MET-2 partners (fig. S4A): LIN-65 is a 100kDa protein and the most abundant interactor of MET-2 (fig. S4B); B0336.5 codes for a smaller protein (~30kDa) and had lower spectral counts, but similar protein coverage as LIN-65

(fig. S4A). We renamed B0336.5 as *arle-14* for ARL14 Effector Protein, as explained below.

To test the role of the MET-2 binding partners in H3K9me deposition, we analyzed loss-of-function mutants. *lin-65* mutants had dramatically reduced levels of H3K9me1 and H3K9me2, and low H3K9me3 (Fig. 4A, B). Wild-type embryos had puncta of H3K9me3 and a large standard deviation of line-scan values, whereas *met-2* and *lin-65* mutants each had dispersed H3K9me3 with a more uniform distribution in the nucleus (Fig. 4C-D). Thus, *lin-65* mutants resembled *met-2* mutants, suggesting it is an essential cofactor. On the other hand, *arle-14* mutants had reduced H3K9me1/me2 levels and largely normal H3K9me3 (Fig. 4A, B). These mutants were similar to a partial loss of *met-2* activity, suggesting *arle-14* is less critical than *lin-65*.

lin-65 and *arle-14* resembled *met-2* mutants in two additional assays. First, an important role of MET-2 is to silence repetitive DNA (*19*, *21*). RNAs for two repeats were de-repressed by *arle-14* mutations and, to a greater degree, by *lin-65* (Fig. 4E). Second, de-repressed repeats lead to a mortal germline phenotype for *met-2* mutants at 26˚C (*21*). Similarly, *lin-65* mutants became sterile after a single generation, and *arle-14* mutants after two generations (n=80 worms, Generation 1: 20% sterility, Generation 2: 100% sterility). These results indicate that LIN-65 and ARLE-14 are *bona fide* binding partners for MET-2 and contribute to its functions.

To address whether LIN-65 and ARLE-14 contribute to the onset of heterochromatin formation, we examined their expression during embryogenesis. We generated an antibody against bacterially-produced ARLE-14 and inserted a 3xFLAG tag at the carboxyl terminus of endogenous LIN-65 by Crispr. Both proteins behaved similarly

to MET-2: they were enriched in the cytoplasm from the one-cell stage through the eight-cell stage, but gradually moved into nuclei thereafter; total levels did not change (fig. S4C, D). During gastrulation, we observed concentrated hubs of MET-2, LIN-65 and ARLE-14 emerge within nuclei (Fig. 4F, H, I, J). The hubs were visible by eye within nuclei and defined more rigorously with an intensity threshold (Figure 4F). H3K9me2, MET-2, LIN-65 and ARLE-14 co-localized in hubs, and these excluded the activating mark H3K4me3 (Fig. 4G). MET-2 and its binding partners never excluded each other in the nucleus, but we frequently observed intense hubs of one protein that did not overlap with each other (Fig. 4G). This result suggests that although these proteins bind each other, they are not always co-localized in the cell, and that binding interactions may be specific to certain regions or functions.

The antibody stains suggested that MET-2 could bind LIN-65 and ARLE-14 in either the cytoplasm or the nucleus, but imaging of proteins under the light microscope lacks the resolution to define where binding occurs. We took advantage of the Proximity Ligation Assay (PLA), which detects pairs of proteins when they are within ~30 nm of each other, to investigate MET-2 binding to its partners. Positive and negative controls demonstrated that our PLA signals were specific (fig. S4E-F). At the earliest stages of embryogenesis, we observed MET-2 PLA^{+} signal with LIN-65 and ARLE-14 in the cytoplasm but rarely in the nucleus (~5% nuclear; Fig. 4K-M). As embryos matured, we continued to detect PLA signals in the cytoplasm but also observed signal within nuclei for MET-2 with both LIN-65 (~53%) and ARLE-14 (~67%). These results reveal that MET-2 interacts closely with LIN-65 and ARLE-14, and that the interacting proteins accumulate in nuclear hubs over time.

To begin to address how ARLE-14 contributes to the deposition of H3K9me2 by MET-2, we examined MET-2 in wild-type and *arle-14* embryos. Neither the localization nor the level of MET-2 changed in *arle-14* mutants (Fig. 5A-B). On the other hand, expression of ARLE-14 tracked extremely well with MET-2 (Fig. 5C-D). In wild-type embryos, ARLE-14 was predominantly nuclear but in *met-2* mutants lacking MET-2 protein, ARLE-14 was lost, suggesting that MET-2 is required for ARLE-14 stability or accumulation. These data indicate that *arle-14* is not required to localize MET-2 into nuclei.

Next, we used ChIP-seq to determine whether *arle-14* affects the genome-wide location of H3K9me2 or MET-2. The distribution of H3K9me2 was normal in *arle-14* mutants (wild-type vs. *arle-14* gave a genome-wide correlation of 0.86 and 0.66 for two independent experiments) (Fig. 5E-F). We conclude that ARLE-14 is not required to target MET-2 in the genome. We also examined the level of H3K9me2 quantitatively. ChIP-Seq experiments are rarely quantitative, due to the methods of sample isolation and library preparation (see Methods). Thus, while ChIP-Seq can reveal where H3K9me2 is located in the genome, it does not reveal how much. To quantify the level of H3K9me2, we used ChIP-qPCR on material prior to DNA amplification and normalized to input DNA. H3K9me2 ChIP-qPCR confirmed the decrease in H3K9me2 levels in *arle-14* mutants (Fig. 5G), similar to immunostaining results (Fig. 4A). These findings indicate that H3K9me2 is in the right places in the genome, but at a reduced level.

Quantitative analysis by ChIP-qPCR revealed a two-fold decrease in MET-2::GFP binding to known genomic targets in *arle-14* mutants (Fig. 5H). These data show that *arle-*

14 is required for robust association of MET-2 with chromatin. The reduction in chromatin-associated MET-2 may explain the low level of H3K9me2 in *arle-14* mutants.

The reduction in chromatin-associated MET-2 and H3K9me2 suggested that *arle-14* would be important for timing H3K9me2 in early embryos. We tested this idea with stains of *arle-14* mutants and quantified the level of H3K9me2 with histone H3 normalization. From the 5-20 cell to the 51-100 cell stage, we observed a linear accumulation of H3K9me2 with a slope of 0.41 (R^2=0.99) for the wild type and a slope of 0.15 (R^2=0.98) for *arle-14* (Fig. 5I-J). From the 1-4 cell to the 5-20 cell stage, H3K9me2 appeared to accumulate more slowly with a slope of 0.11 for the wild type and 0.02 for *arle-14*. These data indicate that *arle-14* is required for accumulation of H3K9me2 at every stage analyzed and suggest that the rate of deposition is slowest during the first few cell divisions.

Prior to this study, ARLE-14 was an uncharacterized *C. elegans* protein with homology to ADP Ribosylation Factor Like 14 Effector Protein (ARL14EP; Fig. 5K). In vertebrates, the only published function for ARL14EP is in the cytoplasm (*22*). However, the Protein Atlas shows ARL14EP in the nuclei of many human tissues (www.proteinatlas.org). We surveyed large-scale interaction databases (*23–25*) and uncovered an interaction between ARL14EP and SETDB proteins in both humans and *Drosophila* (Fig. 5L). We suggest that, in addition to its cytoplasmic function, ARLE-14 and its orthologues function in nuclei with SETDB methyltransferases.

Next, we examined LIN-65. In *lin-65* mutants, MET-2 remained cytoplasmic (Fig. 6A, fig. S5A), as did ARLE-14 (Fig. 5C). MET-2 levels did not decrease in *lin-65* mutants (fig. S5B), indicating that LIN-65 affected the subcellular distribution of MET-2 but not its

stability. These data show that LIN-65 is required for the timely accumulation of MET-2 within nuclei. MET-2, LIN-65 and ARLE-14 likely bind in a complex together because MET-2 requires LIN-65 for nuclear localization, whereas ARLE-14 requires MET-2 for both nuclear localization and cellular accumulation.

MET-2 is required for nuclear accumulation of LIN-65 in adult worms upon mitochondrial stress (*18*). We wondered if a similar relationship between MET-2 and LIN-65 might exist in embryos in the absence of mitochondrial stress. LIN-65::3xFLAG was nuclear in wild-type embryos, but cytoplasmic in *met-2* mutants (fig. S5C). These results show that LIN-65 and MET-2 are dependent on each other for nuclear localization.

The NLS experiment suggested that nuclear accumulation of MET-2 might be rate-limiting for H3K9me2 and heterochromatin formation. To test this idea further, we reduced the dose of MET-2 or LIN-65 by examining embryos from *met-2/+* or *lin-65/+* heterozygotes. Embryos from *met-2/+* mothers behaved like wild-type, with normal levels and distribution of MET-2 and H3K9me2 (fig. S5D, E), suggesting that MET-2 is dosage compensated. A half dose of *lin-65* lead to reduced accumulation of MET-2::GFP within nuclei and an increase of cytoplasmic MET-2 (fig. S5F). The slope of H3K9me2 was reduced by half, from 0.32 in the wild type (R^2=0.99) to 0.16 in the *lin-65* heterozygotes (R^2=0.99). H3K9me3 was also reduced but less dramatically (from a slope of 0.22 R^2=0.96) to 0.18 R^2=0.95). Gastrula embryos had approximately half the level of age-matched controls (Fig. 6C-F, p=1.5 x10^{-14} for H3K9me2, p=8.8 x10^{-13} for H3K9me3). These results indicate that LIN-65 is rate-limiting for nuclear accumulation of MET-2 and H3K9me.

lin-65 belongs to the synMuv B subclass of regulators, which are involved in chromatin regulation and transcriptional repression (*26*). Although *lin-65* had been annotated as a novel protein (*18*, *27*), we found similarities between LIN-65 and the co-factor Activating Transcription Factor 7-Interacting Protein (ATF7IP; Fig 6G). Like ATF7IP, LIN-65 has a high-probability coiled-coil region predicted by PCOILS (CC) and a high-confidence beta-sandwich in the C-terminus (βS) embedded within extensive disordered sequences (fig. S5G-H). Like LIN-65, ATF7IP binds and localizes SETDB1 to nuclei (*28–30*). Despite these similarities, LIN-65 is not an obvious orthologue of ATF7IP and may be an example of convergent evolution.

DISCUSSION

De novo generation of heterochromatin domains is a conserved feature of embryogenesis, but it was previously unclear how timing was established. This study revealed that heterochromatin onset depends on the gradual accumulation of MET-2 within nuclei. Relocation depends on two MET-2 binding partners: LIN-65 is critical for MET-2 nuclear localization, and ARLE-14 is important for MET-2 to associate with chromatin. Naturally, these activities do not rule out additional roles for MET-2 regulation by LIN-65 and ARLE-14.

Similar to *C. elegans*, mammals and *Drosophila* rebuild heterochromatin domains during embryogenesis (*1*, *31*). More generally, lack of heterochromatin domains appears to be a feature of undifferentiated cells, including embryonic stem cells and planarian neuroblasts, and differentiation involves re-establishing heterochromatin (*1*). Examination

of previous studies suggest murine SetDB1 is cytoplasmically enriched in early embryos, but its function has been difficult to address due to early lethality (*32*, *33*). An intriguing idea is that nuclear localization of SETDB with ATF7IP and ARL14EP initiates heterochromatin formation in other animals as well.

The localization of MET-2 in *C. elegans* cells had previously been controversial. One study argued MET-2 was cytoplasmic (*13*) while another demonstrated that MET-2 was required for nuclear localization of LIN-65 under mitochondrial stress conditions, but MET-2 itself was assumed to be cytosolic (*18*). On the other hand, ChIP experiments had suggested that MET-2 associated with chromatin, implying a nuclear focus (*19*)(*20*). One possibility is that excess MET-2 may overwhelm LIN-65 and accumulate in the cytosol under conditions where native MET-2 would be nuclear.

What is the function of de novo H3K9me and heterochromatin formation during embryogenesis? It has been proposed that generation of heterochromatin is critical for loss of pluripotency and restriction of cell fate during gastrulation (*34*). In support of this notion, H3K9 methylation can act as an epigenetic barrier against reprogramming cells into a pluripotent state (*35*). In addition, absence of heterochromatin in early embryos may provide a brief window where repetitive sequences are transcribed, which is a pre-requisite for initiating silencing (*36*).

Alterations in H3K9 methylation has been observed in polycystic ovary syndrome (PCOS), a frequent cause of infertility in women (*37*, *38*). PCOS leads to a range of defects including aberrant oocyte morphology and an increased incidence of miscarriage (*39*). ARL14EP was identified by GWAS as a promising candidate for PCOS (*40*). It is

intriguing to speculate that there may be a link between ARL14EP and H3K9 methylation in PCOS.

MATERIALS AND METHODS

Number of experiments and embryos surveyed.

For imaging experiments, first, many embryos were surveyed under the microscope through the eye piece and general trends noted. Then a random subset of embryos was imaged and analyzed more deeply, with quantitation. Details of analysis are described separately in the Image analysis section, and the analysis gave the same qualitative result as the trends observed in the initial survey.

Fig.1C. >50 embryos were surveyed for each histone mark. At least 5 wild-type embryos from each developmental stage were imaged and analyzed in N=3 experiments.

Fig. 2A. TEM in *met-2* mutants was done in N=2 experiments. For the latest stages of embryogenesis (>200cells), in the first experiment: 49 nuclei across 8 embryos, and in the second experiment: 71 nuclei across 13 embryos were surveyed.

Fig. 3A. >100 embryos were surveyed. A total of 37 embryos were imaged and analyzed in N=3 experiments.

Fig. 3D. >50 embryos were surveyed for each strain.14 wild-type and 14 NLS embryos were imaged and analyzed in N=3 experiments.

Fig. 3E. >50 more embryos for each strain were surveyed. 25 wild-type and 34 NLS embryos were imaged and analyzed in N=3 experiments.

Fig. 4A. We analyzed the following number of embryos in N=3 experiments: H3K9me1: WT vs. *met-2(ok2307)* (5, 7), WT vs. *lin-65(n3441)* (8, 12), WT vs. *arle-14(tm6845)* (6, 7). H3K9me2: WT vs. *met-2(ok2307)* (11, 20), WT vs. *lin-65(n3441)* (10, 13), WT vs. *arle-14(tm6845)* (22, 21). H3K9me3: WT vs. *met-2(ok2307)* (14, 12), WT vs. *lin-65(n3441)* (6,6), WT vs. *arle-14(tm6845)* (5,6).

Fig. 4I. 41 embryos were analyzed in N=3 experiments.

Fig. 4J. 30 embryos were analyzed in N=3 experiments.

Fig. 4K. For MET-2/ARLE-14 PLA, a total of 20 embryos were analyzed in N=3 experiments. For MET-2/LIN-65 PLA, a total of 28 embryos were analyzed in N=3 experiments.

Fig. 5A. >30 mutant embryos were surveyed. 31 wild-type embryos and 21 *arle-14(tm6845)* mutant embryos were imaged and analyzed in N=3 experiments.

Fig. 5C. >50 embryos were surveyed for each strain.11 wild-type vs. 11 *lin-65(n3441)* mutant embryos, 8 wild-type vs. 4 *met-2(ok2307)* mutant embryos were imaged and analyzed in N=3 experiments.

Fig. 5E. 2 biological replicates were processed in parallel.

Fig. 5I. >40 embryos were surveyed for each strain.10 wild-type and 19 *arle-14(tm6845)* mutant embryos were imaged and analyzed in N=3 experiments.

Fig. 6A. >100 *lin-65* embryos were surveyed. 14 wild-type and 31 *lin-65* embryos were imaged and analyzed in N=3 experiments.

Fig. 6C. >50 *lin-65* +/- embryos were surveyed. 22 wild-type and 25 *lin-65* +/- embryos were analyzed in N=3 experiments.

Fig. 6E. >50 *lin-65* +/- embryos were surveyed. 14 wild-type and 16 *lin-65* +/- embryos were analyzed in N=3 experiments.

Strains

Worms were maintained at 20ºC, unless stated otherwise. A full list of strains used in this study, their maintenance conditions and construction of strains generated in this study can be found in the supplement.

Antibody staining

Details of the staining protocol and a full list of antibodies used in this study are available in the supplement, together with a description of how antibodies against endogenous MET-2 or ARLE-14 were generated. For mutant configurations, an on-slide wild-type sample was included, marked with a single-copy ZEN-4::GFP tag. On-slide controls allowed better quantitation between different genotypes or stages.

TEM

Adult hermaphrodites were rapidly chilled in liquid nitrogen while exposed simultaneously to very high pressure (2100 bar). This combination preserves the morphology of organelles and finer structures. Frozen samples underwent freeze substitution to deposit osmium tetroxide for contrast and fixation. Worms were embedded and sectioned along the ovary to view multiple embryos in a row. A detailed protocol is available in the supplement.

Proximity Ligation Assay

Sigma Duolink In Situ Kit (DUO92101) was used for this assay. Embryos were fixed as for regular antibody staining. After overnight staining with primary antibodies at 15ºC, the

sample was stained at 37ºC for 1 hour with secondary antibodies that have oligonucleotide probes attached. Connector oligos were hybridized to the probes and served as templates for circularization by enzymatic ligation when in close proximity. The ligation reaction was incubated at 37ºC for 30 minutes. The circularized DNA strands were used for rolling circle amplification (RCA) and the RCA product was detected by hybridizing fluorescently labeled oligos. The RCA reaction was incubated at 37ºC for 100 minutes. After each step, slides were washed with TBS + 0.2% TritonX for 5 minutes. Slides were mounted in DAPI.

Microscopy and image analysis

Histone modifications. Stacks of optical sections were collected with a ZEISS LSM700 or LSM880 Confocal Microscope and analyzed using Volocity Software. Details of the quantitation by Volocity can be found in the supplement. Signal intensity for histone modifications was normalized to signal intensity for unmodified histones for each nucleus. Normalized values were averaged at given embryonic stages and plotted. (Fig. 1D, 2D, 2E, 2J, 3B, 4E, S1D, S3C, S3D).

TEM Image processing. Raw images were processed with Photoshop as 8-bit gray scale images. Images from different preparations were standardized for accurate comparison. The cytoplasm was used to adjust signal intensity range for each image, but image contrast was not altered. Adjusted images were then saved and quantified with Image J by Line scan analysis.

TEM/H3K9me3 Line scan analysis*:* Random lines were drawn across the center of different nuclei, and the intensity measured. Standard deviation was calculated for each individual line. Standard deviation of 30 lines were averaged for each strain and listed on

the plot. A randomly selected line profile for a nucleus is shown as an example (Fig. 2B for TEM and Fig. 4D for H3K9me3). The standard deviation describes the morphology of the nucleus, i.e. a higher standard deviation stems from a more punctate staining pattern that alternates between high and low values (ie electron dense heterochromatin and electron lucent nucleoplasm or H3K9me3 positive and negative regions in the nucleus).

TEM percentage of EDR. A black and white image was created for each nucleus in ImageJ using the thresholding function. The threshold was chosen manually to best reflect EDRs in >200-cell wild-type embryos and was used to quantify all nuclei (threshold: 39-150). The inner nuclear membrane was manually traced to define an outer most ring, and the number of black vs. total pixels within the ring were used to quantify %EDRs.

MET-2/ARLE-14/LIN-65 Line scan analysis: Lines that go through the center of the nucleus were drawn across the cell, and the intensity measured. Each line had 100 bins. The intensity in each bin was averaged for 30 lines, and the average line plotted. Error bars denote the standard error of the mean at each bin (Fig. 3G, 5B, 5D, 6B, S5C, S5F).

Definition and Quantitation of hubs. Nuclear hubs were defined by intensity thresholding in ImageJ. The threshold was selected manually in wild-type nuclei at the 51-100 cell stage and the same threshold was applied to all the images in a given dataset. The intensity measurements for each defined hub were averaged to yield the intensity of “hubs” at given embryonic stages. “Non-hub” was defined as nuclear areas that were below the intensity threshold. The mean intensity in non-hub areas was measured for each nucleus and averaged across 30 nuclei. Non-interphase nuclei were discarded manually. For intensity measurements in the cytosol, at least 4 random areas in the

cytosol was chosen for every cell that was in interphase. The measured intensities were averaged.

Half-dose LIN-65 experiments

lin-65 (n3441) moms were crossed with JAC500 *his-72::mCherry* males. Progeny of *lin-65+/-* heterozygotes marked by mCherry were analyzed. On the same slide, SM2333 containing a single copy of *zen-4::gfp* was used as a wild-type staining control. Mean H3K9me2 or H3K9me3 intensity in each nucleus was quantified using Volocity and the average H3K9me2 or H3K9me3 intensity per nucleus plotted, normalized as described in the staining section.

Biochemistry and Bioinformatics

Detailed protocols for harvesting embryos, Immunoprecipitation (IP), mass spectrometry (MS), RNA expression, ChIP-Seq and analysis of sequencing data can be found in the supplementary materials and methods.

Data access

The ChIP-Seq data from this study has been submitted to the NCBI GEO database with accession number GSE113841. All data needed to evaluate conclusions in the paper are present in the paper and the Supplementary Materials. Additional data available from authors upon request.

REFERENCES

1. J. C. R. Politz, D. Scalzo, M. Groudine, Something silent this way forms: the functional organization of the repressive nuclear compartment. *Annu. Rev. Cell Dev. Biol.* **29**, 241–70 (2013).
2. T. Guven-Ozkan, Y. Nishi, S. M. Robertson, R. Lin, Global Transcriptional

Repression in C. elegans Germline Precursors by Regulated Sequestration of TAF-4. *Cell*. **135**, 149–160 (2008).

3. M. T. Lee, A. R. Bonneau, A. J. Giraldez, Zygotic genome activation during the maternal-to-zygotic transition. *Annu. Rev. Cell Dev. Biol.* **30**, 581–613 (2014).
4. A. Fadloun, A. Eid, M.-E. Torres-Padilla, Mechanisms and dynamics of heterochromatin formation during mammalian development: closed paths and open questions. *Curr. Top. Dev. Biol.* **104**, 1–45 (2013).
5. T. Yuzyuk, T. H. I. Fakhouri, J. Kiefer, S. E. Mango, The polycomb complex protein mes-2/E(z) promotes the transition from developmental plasticity to differentiation in C. elegans embryos. *Dev. Cell*. **16**, 699–710 (2009).
6. T. H. I. Fakhouri, J. Stevenson, A. D. Chisholm, S. E. Mango, Dynamic chromatin organization during foregut development mediated by the organ selector gene PHA-4/FoxA. *PLoS Genet.* **6** (2010), doi:10.1371/journal.pgen.1001060.
7. H. G. Davies, Electron-microscope observations on the organization of heterochromatin in certain cells. *J. Cell Sci.* **3**, 129–150 (1968).
8. D. H. Hall, E. Hartwieg, K. C. Q. Nguyen, Modern electron microscopy methods for C. elegans. *Methods Cell Biol.* **107**, 93–149 (2012).
9. D. Cmarko, P. J. Verschure, A. P. Otte, R. van Driel, S. Fakan, Polycomb group gene silencing proteins are concentrated in the perichromatin compartment of the mammalian nucleus. *J. Cell Sci.* **116**, 335–343 (2002).
10. M. Wirth *et al.*, HIS-24 linker histone and SIR-2.1 deacetylase induce H3K27me3 in the Caenorhabditis elegans germ line. *Mol. Cell. Biol.* **29**, 3700–9 (2009).
11. J. C. Rice *et al.*, Histone Methyltransferases Direct Different Degrees of Methylation to Define Distinct Chromatin Domains. *Mol. Cell*. **12**, 1591–1598 (2003).
12. J. B. Bessler, E. C. Andersen, A. M. Villeneuve, Differential localization and independent acquisition of the H3K9me2 and H3K9me3 chromatin modifications in the Caenorhabditis elegans adult germ line. *PLoS Genet.* **6**, e1000830 (2010).
13. B. D. Towbin *et al.*, Step-wise methylation of histone H3K9 positions heterochromatin at the nuclear periphery. *Cell*. **150**, 934–47 (2012).
14. L. B. Bender, R. Cao, Y. Zhang, S. Strome, The MES-2/MES-3/MES-6 complex

and regulation of histone H3 methylation in C. elegans. *Curr Biol*. **14**, 1639–1643 (2004).

15. G. Poulin, Y. Dong, A. G. Fraser, N. A. Hopper, J. Ahringer, Chromatin regulation and sumoylation in the inhibition of Ras-induced vulval development in Caenorhabditis elegans. *EMBO J.* **24**, 2613–23 (2005).
16. E. C. Andersen, H. R. Horvitz, Two C. elegans histone methyltransferases repress lin-3 EGF transcription to inhibit vulval development. *Development*. **134**, 2991–9 (2007).
17. J. Garrigues, S. Sidoli, B. Garcia, S. Strome, Defining heterochromatin in C. elegans through genome-wide analysis of the heterochromatin protein 1 homolog HPL-2. *Genome Res.*, 1–14 (2014).
18. Y. Tian *et al.*, Mitochondrial Stress Induces Chromatin Reorganization to Promote Longevity and UPRmt. *Cell*. **165**, 1197–1208 (2016).
19. A. N. McMurchy *et al.*, A team of heterochromatin factors collaborates with small RNA pathways to combat repetitive elements and germline stress. *Elife*. **6**, e21666 (2017).
20. T. Patel, O. Hobert, Coordinated control of terminal differentiation and restriction of cellular plasticity. *Elife*. **6**, e24100 (2017).
21. P. Zeller *et al.*, Histone H3K9 methylation is dispensable for Caenorhabditis elegans development but suppresses RNA:DNA hybrid-associated repeat instability. *Nat. Genet.* **48**, 1385–1395 (2016).
22. P. Paul *et al.*, A Genome-wide Multidimensional RNAi Screen Reveals Pathways Controlling MHC Class II Antigen Presentation. *Cell*. **145**, 268–283 (2011).
23. L. Giot *et al.*, A protein interaction map of Drosophila melanogaster. *Science*. **302**, 1727–36 (2003).
24. K. G. Guruharsha *et al.*, A protein complex network of Drosophila melanogaster. *Cell*. **147**, 690–703 (2011).
25. T. Rolland *et al.*, A Proteome-Scale Map of the Human Interactome Network. *Cell*. **159**, 1212–1226 (2014).
26. D. S. Fay, J. Yochem, The SynMuv genes of Caenorhabditis elegans in vulval development and beyond. *Dev. Biol.* **306**, 1–9 (2007).

27. C. J. Ceol, F. Stegmeier, M. M. Harrison, H. R. Horvitz, Identification and classification of genes that act antagonistically to let-60 Ras signaling in Caenorhabditis elegans vulval development. *Genetics*. **173**, 709–26 (2006).
28. H. Wang *et al.*, mAM facilitates conversion by ESET of dimethyl to trimethyl lysine 9 of histone H3 to cause transcriptional repression. *Mol. Cell*. **12**, 475–487 (2003).
29. T. Ichimura *et al.*, Transcriptional repression and heterochromatin formation by MBD1 and MCAF/AM family proteins. *J. Biol. Chem.* **280**, 13928–35 (2005).
30. C. M. Koch, M. Honemann-Capito, D. Egger-Adam, A. Wodarz, R. Fawcett, Windei, the Drosophila Homolog of mAM/MCAF1, Is an Essential Cofactor of the H3K9 Methyl Transferase dSETDB1/Eggless in Germ Line Development. *PLoS Genet.* **5**, e1000644 (2009).
31. K. Yuan, P. H. O'Farrell, TALE-light imaging reveals maternally guided, H3K9me2/3-independent emergence of functional heterochromatin in Drosophila embryos. *Genes Dev.* **30**, 579–93 (2016).
32. J. E. Dodge, Y.-K. Kang, H. Beppu, H. Lei, E. Li, Histone H3-K9 methyltransferase ESET is essential for early development. *Mol. Cell. Biol.* **24**, 2478–86 (2004).
33. S. Cho, J. S. Park, S. Kwon, Y.-K. Kang, Dynamics of Setdb1 expression in early mouse development. *Gene Expr. Patterns*. **12**, 213–218 (2012).
34. A. Gaspar-Maia, A. Alajem, E. Meshorer, M. Ramalho-Santos, Open chromatin in pluripotency and reprogramming. *Nat. Rev. Mol. Cell Biol.* **12**, 36–47 (2011).
35. J. S. Becker, D. Nicetto, K. S. Zaret, H3K9me3-Dependent Heterochromatin: Barrier to Cell Fate Changes. *Trends Genet.* (2015), doi:10.1016/j.tig.2015.11.001.
36. D. Moazed, Small RNAs in transcriptional gene silencing and genome defence. *Nature*. **457**, 413–420 (2009).
37. L. Li, K.-H. Baek, Molecular genetics of polycystic ovary syndrome: an update. *Curr. Mol. Med.* **15**, 331–42 (2015).
38. F. Eini *et al.*, Intracytoplasmic oxidative stress reverses epigenetic modifications in polycystic ovary syndrome. *Reprod. Fertil. Dev.*, 2313–2323 (2017).
39. S. Palomba, J. Daolio, G. B. La Sala, Oocyte Competence in Women with

Polycystic Ovary Syndrome. *Trends Endocrinol. Metab.* **28**, 186–198 (2017).
40. M. G. Hayes *et al.*, Genome-wide association of polycystic ovary syndrome implicates alterations in gonadotropin secretion in European ancestry populations. *Nat. Commun.* **6**, 7502 (2015).

Acknowledgements. We thank A. Schier, D. Moazed and the Mango lab for comments on the manuscript, S. Von Stetina for *zen-4::gfp,* J. Calarco and A. Norris for *his-72::mCherry,* the Harvard Center for Biological Imaging, K. Nguyen and B. Raja for their help on TEM procedures, Maine Lab members, especially Xia Xu, for their helpful input. We acknowledge support from the NIH (R37GM056264 to SEM, RO1 GM089818 to EMM, and R24OD010943 to DHH), the John D. and Catherine T. MacArthur Foundation and Harvard University to SEM, the AAUW International Fellowship to BM. BDO, JJM, and JRY were supported by the National Institute of General Medical Sciences (8 P41 GM103533). Some strains were provided by the Caenorhabditis Genetics Center, funded by NIH P40OD010440.

Author contributions. BM and SEM designed and conducted the study and wrote the manuscript. DHH performed TEM. HMC performed TEM image processing. JJM, BDO and JRY performed proteomics. BY, SKR and EMM generated the MET-2 antibody and *met-2* Crispr and MosSCI strains. JMG analyzed the H3K9me2 ChIP-Seq data. Authors have no competing interests.

Supplementary Materials

Supplementary Materials and Methods

Supplementary References

Supplementary Figures 1-5

Supplementary Table 1

FIGURE LEGENDS

Fig. 1. Heterochromatin and H3K9me domains are established during embryogenesis.
A. Time line of *C. elegans* embryogenesis. Stages are color-coded: light green (<20 cell, pre-gastrula), green (21-200 cell, gastrula), dark green (200-500 cell, late stage). Morphogenesis starts after the 500-cell stage and was not analyzed in this study.
B. Transmission electron micrographs (TEM) of representative nuclei from wild-type embryos (Scale bar, 1 µm).
C. Survey of histone modifications. Representative single nuclei at designated embryonic stages stained for histones and DNA (Scale bar, 2 µm).
D. Quantitation of histone modifications normalized to total histone H3. Error bars denote standard error of the mean.

Fig. 2. H3K9 methyltransferase MET-2/SETDB1 is required for heterochromatin formation.
A. TEM of representative nuclei from wild-type (WT) or *met-2* embryos (Scale bar, 1 µm).
B. TEM line-scan analysis for WT (black) or *met-2* (magenta) nuclei and the standard deviation (stdev). Line scan for a single nucleus is shown as an example.
C. Proportion of pixels within EDRs at the 200-cell stage**.** Error bars denote standard error of the mean.
D. Contrast of the cytosol in wild-type vs. *met-2* mutants and intensity thresholding (red) to define electron-dense structures. Wild-type nuclei are marked with green and *met-2* nuclei with magenta.

Fig. 3. Nuclear accumulation of MET-2 determines the onset of H3K9 di-methylation.
A. Embryos stained for MET-2::GFP (upper) and HIS-72::mCherry (lower) at designated stages of embryogenesis (Scale bar, 2 µm).
B-C. Quantitation of nuclear (B) and total (C) MET-2 at designated stages, normalized to HIS-72::mCherry. Error bars denote standard error of the mean.
D-E. Localization of 3xFLAG::MET-2 with a c-Myc NLS compared to 3xFLAG::MET-2 control (D) and corresponding H3K9me2 levels (E). Histone H3 was used as a staining control. Note that H3 appears to be released during mitosis, but we focused on interphase cells.
F. Interphase nuclei showing H3K9me2 levels for the *c-myc* NLS construct compared to on-slide control embryos.
G. 3xFLAG::MET-2 line scans in pre-gastrula embryos (1-4 cell stage) with (red) or without (grey) the *c-myc* NLS. Average of line scans across multiple nuclei are shown and error bars denote standard error of the mean.
H. H3K9me2 levels for the NLS construct (red), normalized to H3 and to wild-type embryos at the 51-100cell stage (grey). Error bars denote standard error of the mean.

Fig. 4. MET-2 and two conserved binding partners form concentrated nuclear hubs at gastrulation.
A. Whole embryos stained with antibodies against methylated H3K9 and pan-histones in wild-type vs. *met-2*, *lin-65* or *arle-14* mutants. H3K9me2 (Kimura 6D11) antibodies were used. Scale bar, 2 µm.
B. H3K9me levels in mutant embryos normalized to on-slide control embryos and to pan-histone. Error bars denote standard error of the mean.
C. Representative single nuclei showing H3K9me3(red) and DAPI(blue) in wild-type vs. *met-2*, *lin-65* or *arle-14* mutants. Scale bar, 2 µm.
D. H3K9me3 line-scan analysis for WT (green), *met-2* (magenta), *lin-65* (orange), *arle-14* (yellow) nuclei and the standard deviation (stdev). Line scan for a single nucleus is shown as an example.
E. Expression of CEREP4 and CEMUDR1 repeat RNAs by RT-qPCR in wild-type vs. *met-2*, *lin-65* or *arle-14* mutant embryos.
F. Definition of hubs by intensity thresholding.
G. Single nuclei showing 3xFLAG::MET-2, LIN-65::3xFLAG and ARLE-14 co-localization in concentrated protein hubs and exclusion of activating mark H3K4me3 (Scale bar 2 µm).
H-J. Representative singe nuclei showing 3xFLAG::MET-2 (D), LIN-65::3xFLAG (I) and ARLE-14 (J) localization at different embryonic stages (Scale bar, 2 µm). Quantitation of signal intensity in nuclear hubs (red), nuclear regions excluding hubs ("non-hub", dark grey) and cytosol (light grey). Error bars denote standard error of the mean.
K. PLA signal showing interactions between MET-2/LIN-65 and MET-2/ARLE-14.
L-M. Percentage of nuclear PLA dots per total dots in embryos for MET-2/LIN-65 and MET-2/ARLE-14 interactions. Error bars denote standard error of the mean.

Fig. 5. ARLE-14 promotes chromatin association of MET-2.
A. Whole embryos showing the distribution of MET-2::GFP in WT vs. *arle-14* mutants (Scale bar 2 µm).
B. Line scan analysis showing the mean MET-2::GFP intensity across embryonic cells in WT vs. *arle-14* mutant embryos. Average of line scans across multiple nuclei are shown and error bars denote standard error of the mean.
C. ARLE-14 antibody staining in wild-type vs *met-2*, *lin-65* and *arle-14* mutants.
D. ARLE-14 line scan quantitation. Average of line scans across multiple nuclei are shown and error bars denote standard error of the mean.
E-F. H3K9me2 ChIP-Seq (logLR) track in wild-type vs. *arle-14* mutant embryos (chromosome III and loci: *rep-1, Y22D7AL.7, grl-16*). 5 wild-type ChIP experiments and 10 *arle-14* mutant ChIP experiments were pooled in for sequencing and results are not quantitative.
G. H3K9me2 ChIP-qPCR in wild-type vs. *arle-14* mutants before combining parallel ChIP experiments together for sequencing. Error bars denote standard error of the mean.
H. MET-2::GFP ChIP-qPCR for wild-type (green) vs. *arle-14* (yellow) mutant embryos. Inset shows H3K4me3 ChIP-qPCR as a control. The y-axis shows normalized %input values for both wild-type and mutants, where the %input value at the H3K4me3 positive

region was set to 1 for both genotypes. %input for MET-2::GFP ChIP was adjusted accordingly. Error bars denote standard error of the mean for N=3 experiments.
I-J. Acquisition of H3K9me2 in wild-type vs. *arle-14* mutants during embryogenesis, with an H3 co-stain (D) and quantitation normalized to H3 (E). Error bars denote standard error of the mean.
K. Amino acid sequence alignment of worm ARLE-14 to the human ARL14EP domain using ClustalX2. Color scheme: Hydrophobic-blue, Positive charge-red, Negative charge-magenta, Polar-green, Cysteines-pink, Glycines-orange, Prolines-Yellow, Aromatic-cyan.
L. Protein interaction map for human ARL14EP from String database (https://string-db.org/). Red box highlights interactions with human SETDB1/2.

Fig. 6. LIN-65 is rate-limiting for H3K9me2 and nuclear MET-2 during embryogenesis.
A. Distribution of MET-2::GFP in wild-type vs. *lin-65* mutants vs. no-GFP wild-type strain (Scale bar, 2 µm). Note that this H3 antibody detects mostly cytosolic histone H3 during mitosis.
B. Line-scan analysis across embryonic nuclei shows mean MET-2::GFP intensity in wild-type (green) vs. *lin-65* (pink) mutants vs. no-GFP control ("-", grey). Average of line scans across multiple nuclei are shown and error bars denote standard error of the mean.
C,E. H3K9me2 and H3K9me3 levels in embryos with a single copy ZEN-4::GFP ("WT", on-slide control) or progeny *of lin-65(+/-)* heterozygous mothers identified by HIS-72::mCherry at designated stages of embryogenesis.
D,F. Quantitation of H3K9me2 and H3K9me3 levels from wild-type (grey) or *lin-65(-/+)* (purple) offspring. Error bars denote standard error of the mean.
G. Domain architecture from HMMR (https://www.ebi.ac.uk/Tools/hmmer/) for human ATF7IP, fly Windei and worm LIN-65 showing disordered (purple), coiled-coil (pink), and beta-sandwich fold (violet) regions.
H. In early embryos, MET-2 (grey), LIN-65 (red) and ARLE-14 (yellow) are enriched in the cytosol, and there is little H3K9me2 or heterochromatin (light green). As embryos mature, MET-2 and interactors gradually accumulate in nuclei, form concentrated nuclear hubs and deposit H3K9me2. MET-2-dependent H3K9 methylation is required to generate heterochromatin domains (compacted, dark green).

Mutlu_fig1

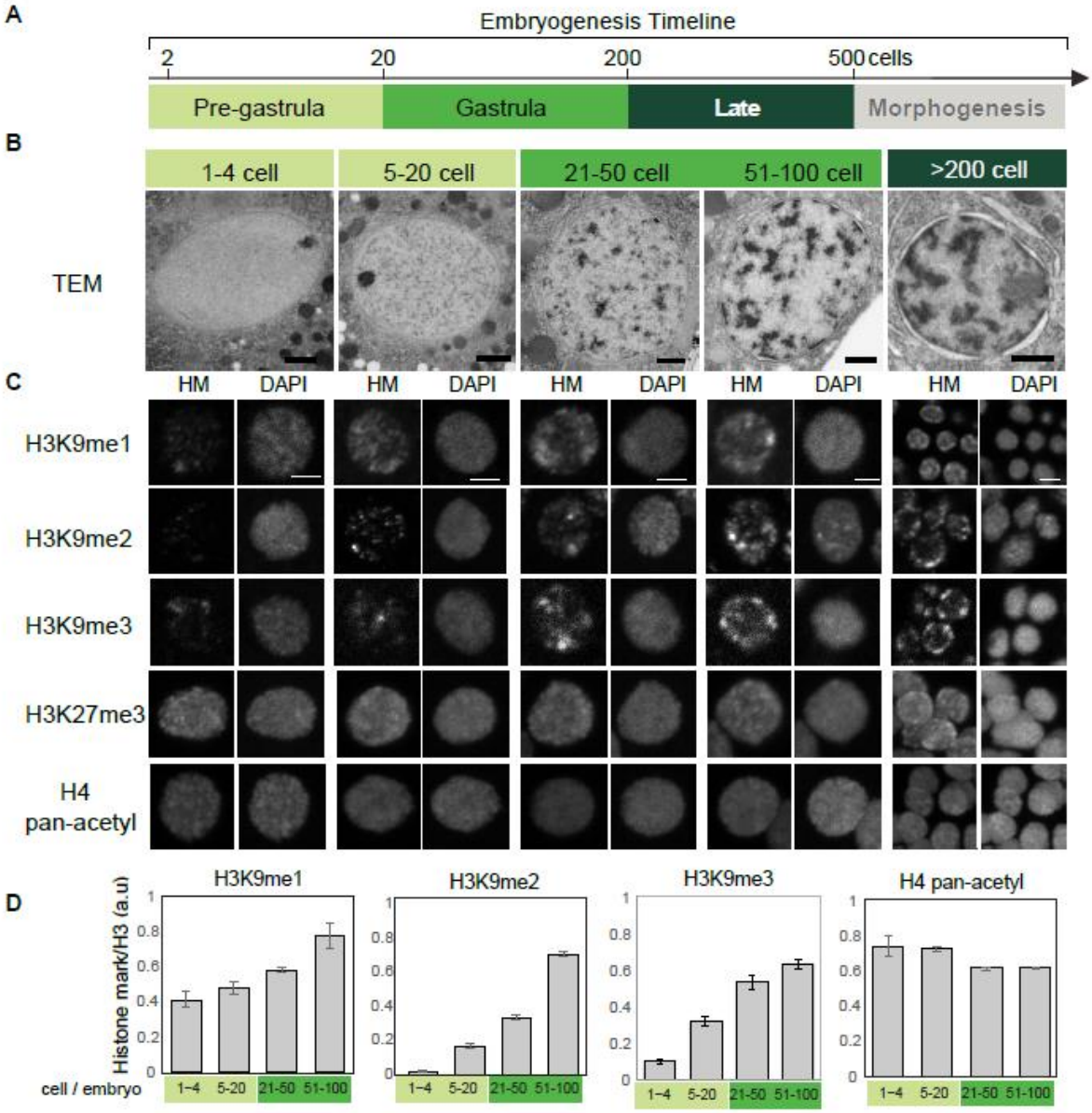
A
Embryogenesis Timeline
2
20
200
500 cells
Pre-gastrula
Gastrula
Late
Morphogenesis
B
1-4 cell
5-20 cell
21-50 cell
51-100 cell
>200 cell
TEM
C
HM
DAPI
H3K9me1
H3K9me2
H3K9me3
H3K27me3
H4
pan-acetyl
D
H3K9me1
H3K9me2
H3K9me3
H4 pan-acetyl
Histone mark/H3 (a.u)
cell / embryo
1-4
5-20
21-50
51-100

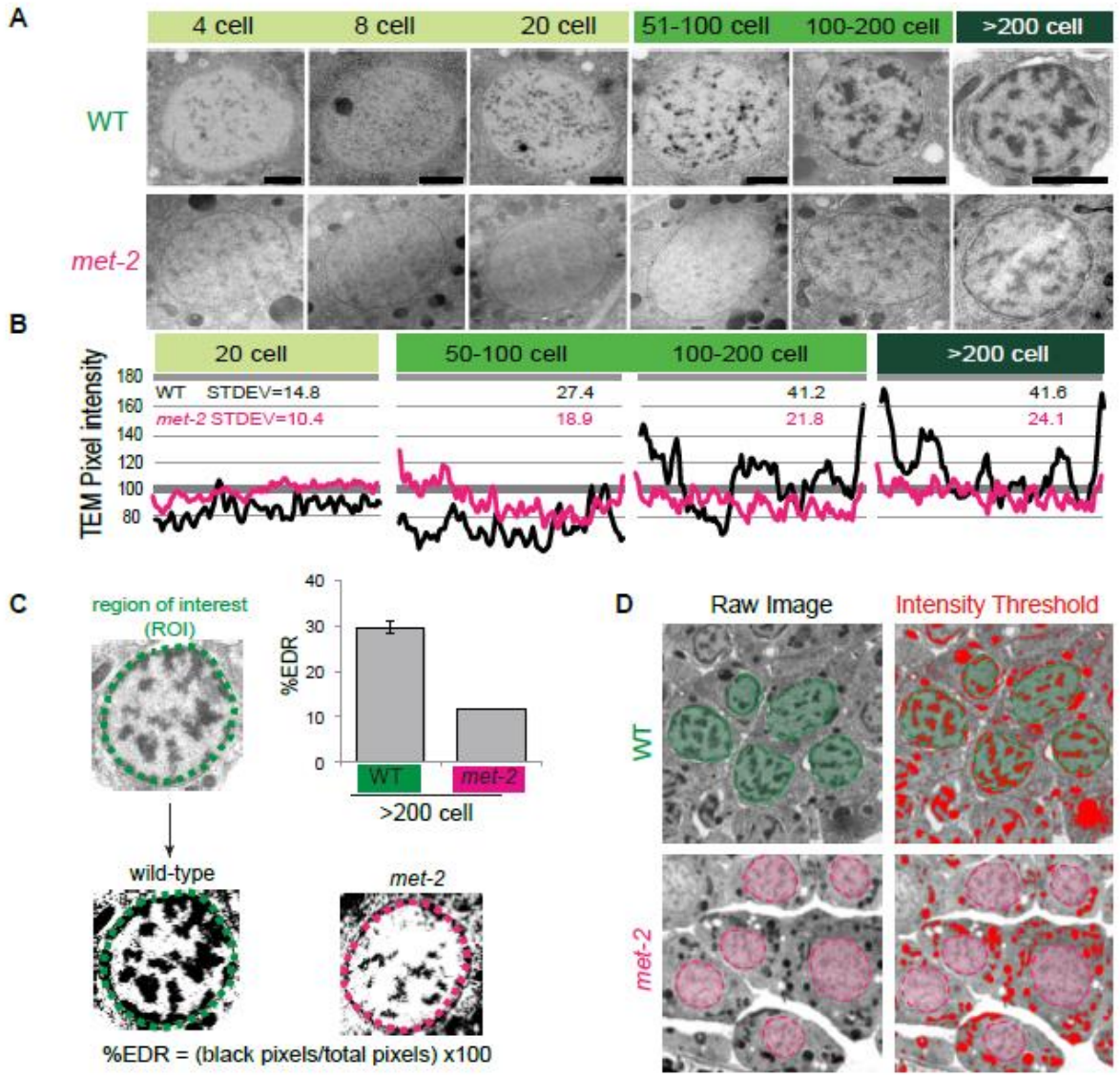
A
4 cell
8 cell
20 cell
51-100 cell
100-200 cell
>200 cell
WT
met-2
B
20 cell
50-100 cell
100-200 cell
>200 cell
TEM Pixel intensity
180
160
140
120
100
80
WT STDEV=14.8
met-2 STDEV=10.4
27.4
18.9
41.2
21.8
41.6
24.1
C
region of interest (ROI)
wild-type
met-2
%EDR
40
30
20
10
0
WT
met-2
>200 cell
%EDR = (black pixels/total pixels) x100
D
Raw Image
Intensity Threshold
WT
met-2

Mutlu_fig3

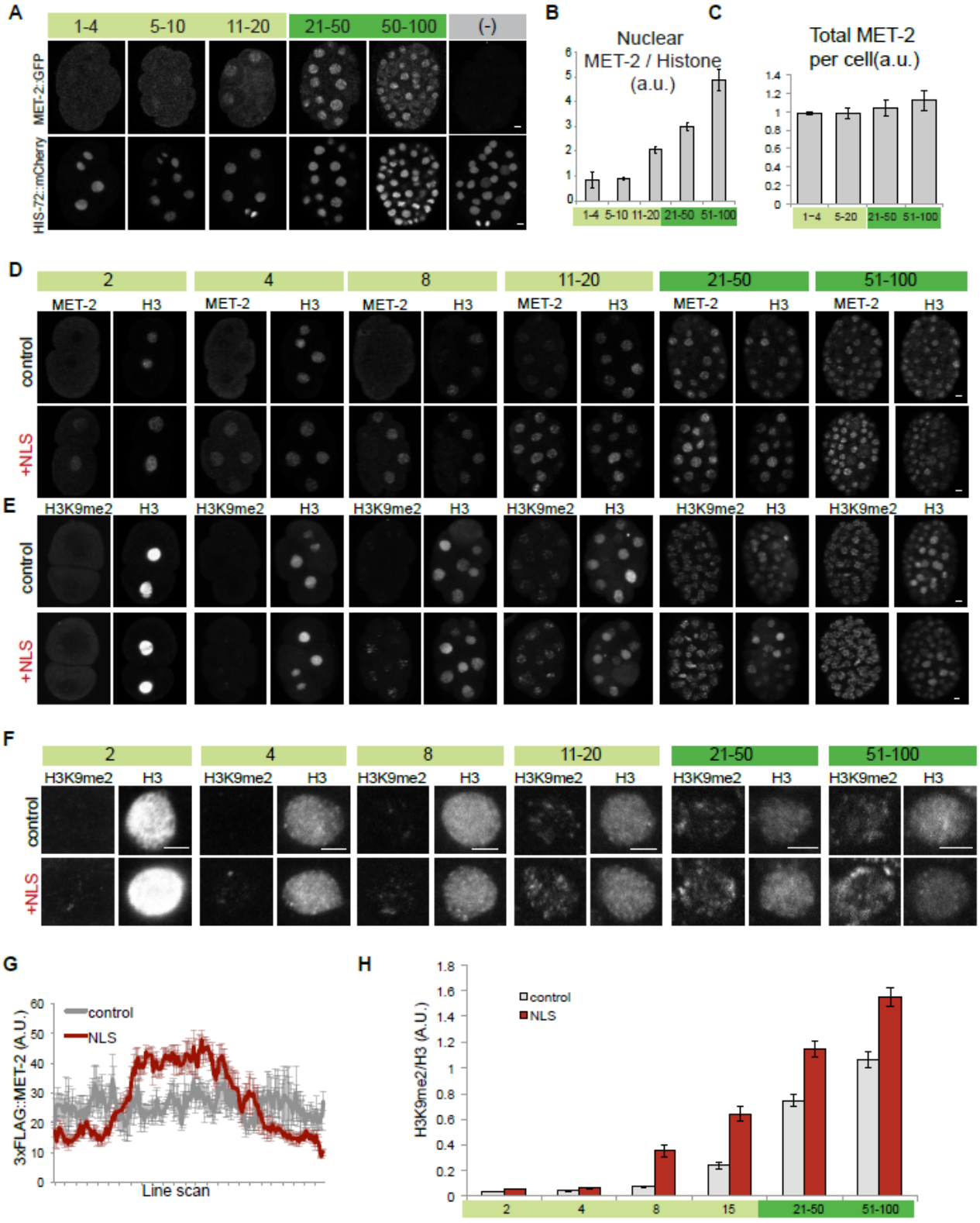
A
1-4
5-10
11-20
21-50
50-100
(-)
MET-2::GFP
HIS-72::mCherry
B
Nuclear
MET-2 / Histone
(a.u.)
1-4 5-10 11-20 21-50 51-100
C
Total MET-2
per cell(a.u.)
1-4 5-20 21-50 51-100
D
2
4
8
11-20
21-50
51-100
MET-2
H3
control
+NLS
E
H3K9me2
H3
control
+NLS
F
2
4
8
11-20
21-50
51-100
H3K9me2
H3
control
+NLS
G
control
NLS
3xFLAG::MET-2 (A.U.)
Line scan
H
control
NLS
H3K9me2/H3 (A.U.)
2
4
8
15
21-50
51-100

Mutlu_fig4

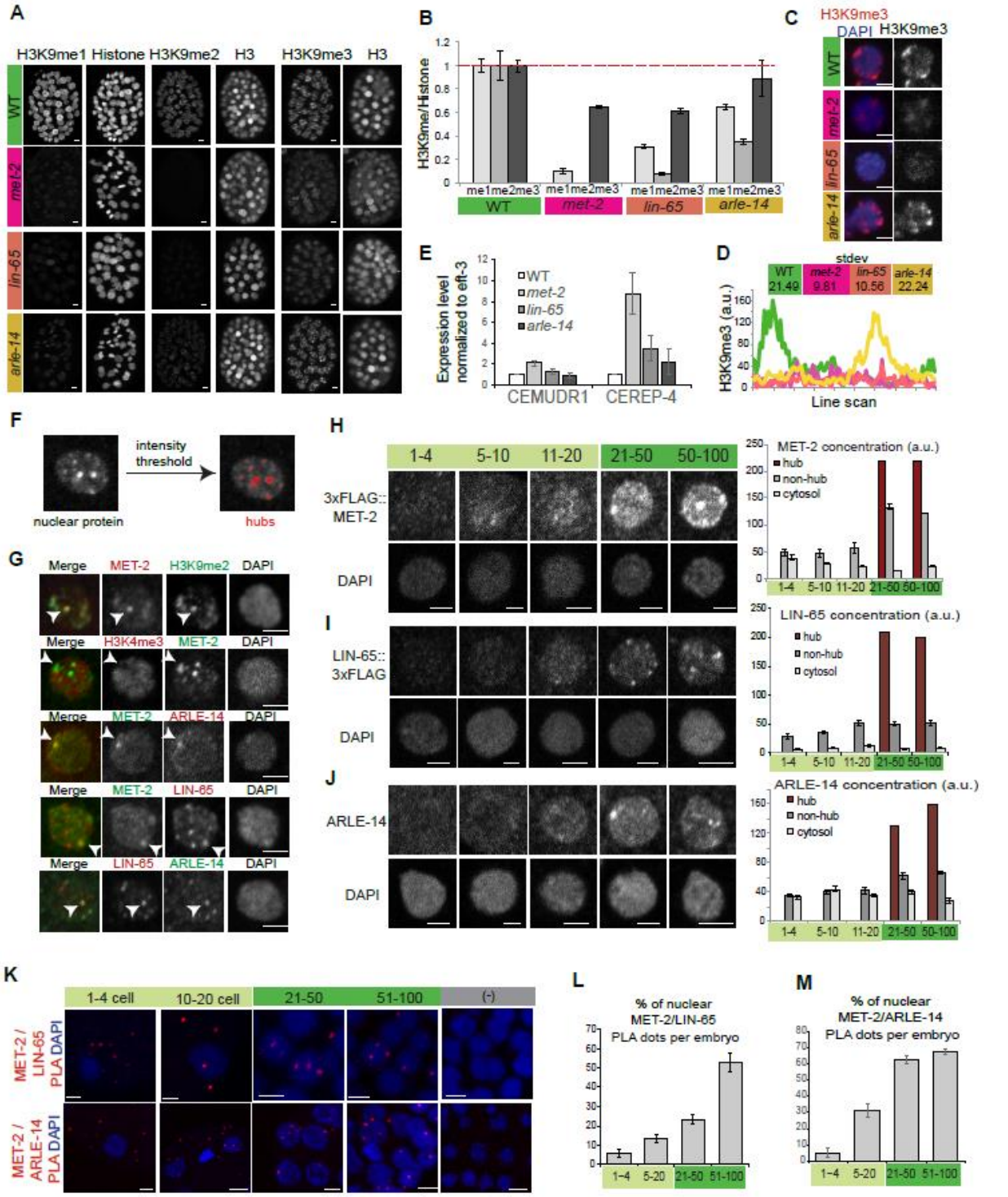
A
H3K9me1 Histone H3K9me2 H3 H3K9me3 H3
WT
met-2
lin-65
arle-14
B
H3K9me/Histone
me1me2me3 me1me2me3 me1me2me3 me1me2me3
WT met-2 lin-65 arle-14
C
H3K9me3
DAPI H3K9me3
WT
met-2
lin-65
arle-14
D
stdev
WT 21.49
met-2 9.81
lin-65 10.56
arle-14 22.24
H3K9me3 (a.u.)
Line scan
E
Expression level normalized to eft-3
WT
met-2
lin-65
arle-14
CEMUDR1 CEREP-4
F
intensity threshold
nuclear protein
hubs
G
Merge MET-2 H3K9me2 DAPI
Merge H3K4me3 MET-2 DAPI
Merge MET-2 ARLE-14 DAPI
Merge MET-2 LIN-65 DAPI
Merge LIN-65 ARLE-14 DAPI
H
1-4 5-10 11-20 21-50 50-100
3xFLAG:: MET-2
DAPI
MET-2 concentration (a.u.)
hub
non-hub
cytosol
I
LIN-65:: 3xFLAG
DAPI
LIN-65 concentration (a.u.)
J
ARLE-14
DAPI
ARLE-14 concentration (a.u.)
K
1-4 cell 10-20 cell 21-50 51-100 (-)
MET-2 / LIN-65 PLA DAPI
MET-2 / ARLE-14 PLA DAPI
L
% of nuclear MET-2/LIN-65 PLA dots per embryo
1-4 5-20 21-50 51-100
M
% of nuclear MET-2/ARLE-14 PLA dots per embryo
1-4 5-20 21-50 51-100

Mutlu_fig5

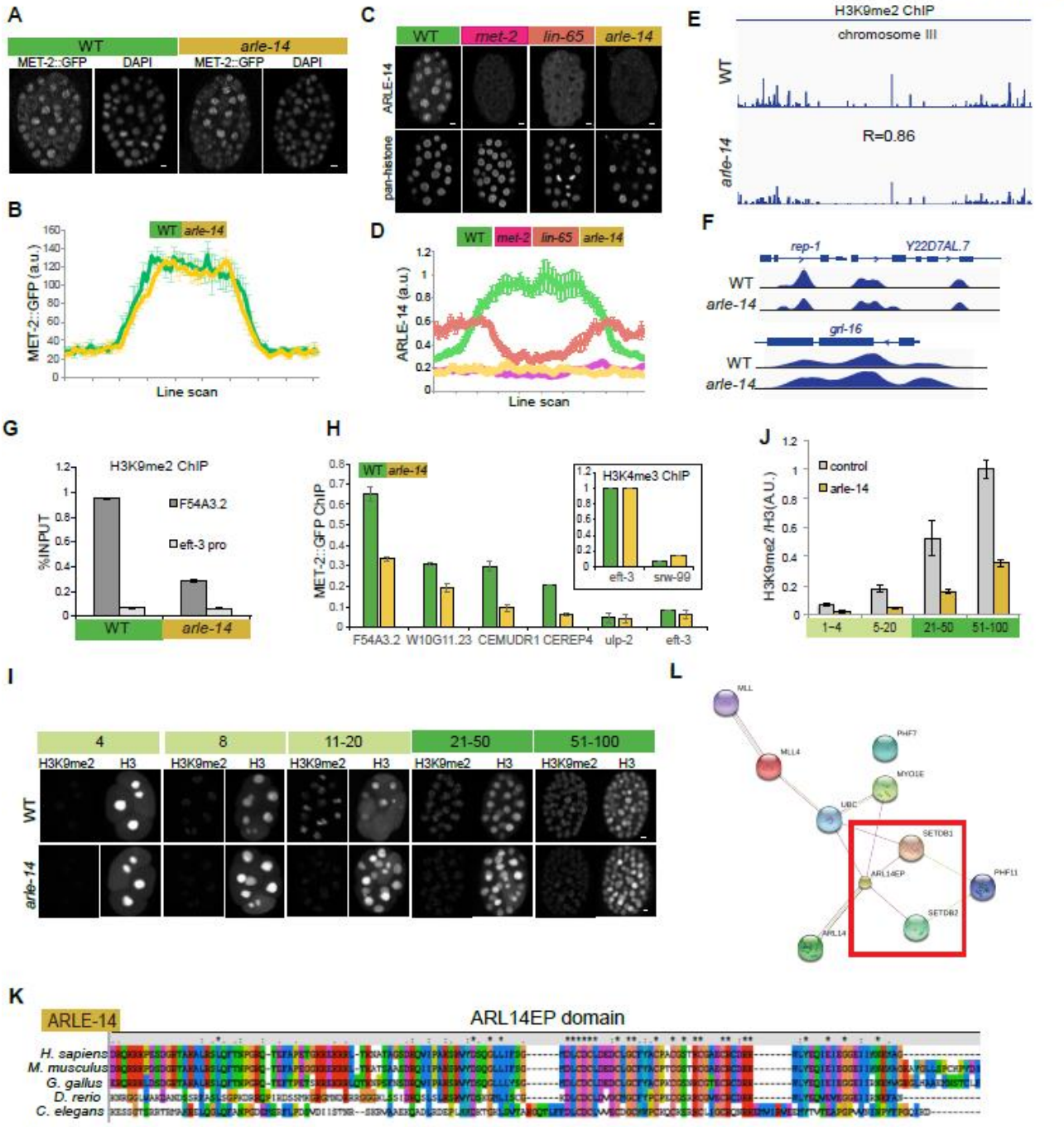
A
WT
arle-14
MET-2::GFP
DAPI
B
MET-2::GFP (a.u.)
Line scan
C
met-2
lin-65
ARLE-14
pan-histone
D
ARLE-14 (a.u.)
E
H3K9me2 ChIP
chromosome III
R=0.86
F
rep-1
Y22D7AL.7
gri-16
G
H3K9me2 ChIP
%INPUT
F54A3.2
eft-3 pro
H
MET-2::GFP ChIP
H3K4me3 ChIP
eft-3
snw-99
F54A3.2
W10G11.23
CEMUDR1
CEREP4
ulp-2
J
control
H3K9me2 /H3(A.U.)
1-4
5-20
21-50
51-100
I
4
8
11-20
21-50
51-100
H3K9me2
H3
L
MLL
MLL4
PHF7
MYO1E
UBC
SETDB1
ARL14EP
PHF11
SETDB2
ARLL4
K
ARLE-14
ARL14EP domain
H. sapiens
M. musculus
G. gallus
D. rerio
C. elegans

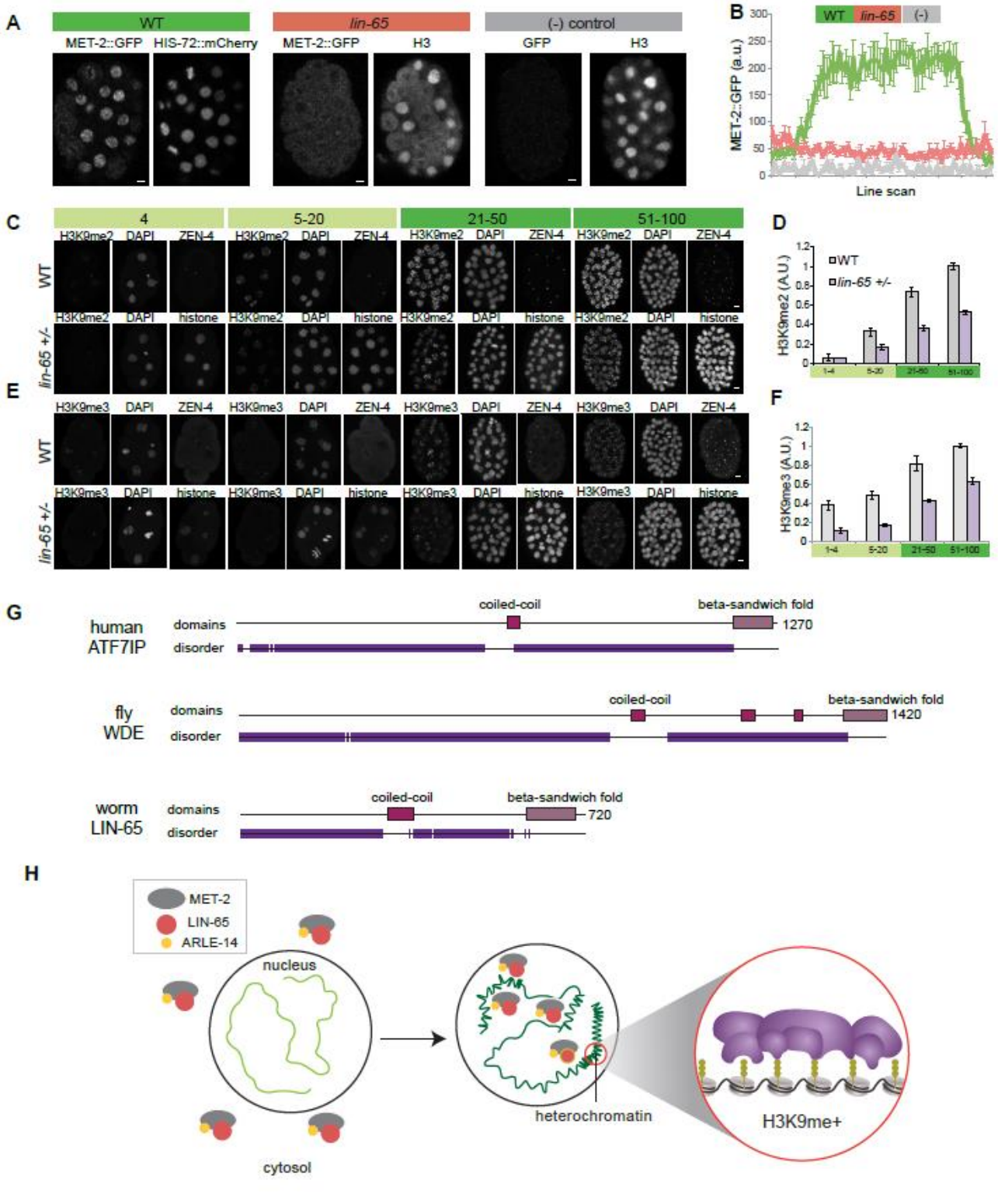
A
WT
lin-65
(-) control
MET-2::GFP
HIS-72::mCherry
MET-2::GFP
H3
GFP
H3
B
WT
lin-65
(-)
MET-2::GFP (a.u.)
Line scan
C
4
5-20
21-50
51-100
H3K9me2
DAPI
ZEN-4
histone
WT
lin-65 +/-
D
WT
lin-65 +/-
H3K9me2 (A.U.)
E
H3K9me3
F
H3K9me3 (A.U.)
G
human ATF7IP
domains
disorder
coiled-coil
beta-sandwich fold
1270
fly WDE
1420
worm LIN-65
720
H
MET-2
LIN-65
ARLE-14
nucleus
cytosol
heterochromatin
H3K9me+